



## Wide-bandgap GaN-based watt-class photonic-crystal lasers

Kei Emoto<sup>1,2</sup>, Tomoaki Koizumi<sup>1,2</sup>, Masaki Hirose<sup>2</sup>, Masahiro Jutori<sup>2</sup>, Takuya Inoue <sup>3</sup>, Kenji Ishizaki<sup>2</sup>, Menaka De Zoysa<sup>3</sup>, Hiroyuki Togawa<sup>1</sup> & Susumu Noda <sup>2,3</sup>✉

Short-wavelength (blue-violet-to-green) lasers with high power and high beam quality are required for various applications including the machining of difficult-to-process materials and high-brightness illuminations and displays. Promising light sources for such applications are wide-bandgap GaN-based photonic-crystal surface-emitting lasers (PCSELS), which are based on two-dimensional resonance in the photonic crystal. Developments of these devices have lagged behind those of longer-wavelength GaAs-based PCSELS, because device designs for achieving robust two-dimensional resonance and a nanofabrication process that avoids introducing disorders have remained elusive for wide-bandgap GaN-based materials. Here, we address these issues and successfully realize GaN-based PCSELS with high, watt-class (>1 W) output power and a circular, single-lobed beam with a very narrow ( $\sim 0.2^\circ$ ) divergence angle at blue wavelengths. In addition, we demonstrate continuous-wave operation with a high output power ( $\sim 320$  mW) and a high beam quality ( $M^2 \sim 1$ ). Our results will enable the use of GaN-based PCSELS in the above-mentioned applications.

<sup>1</sup> Research & Development Laboratory, Stanley Electric Co., Ltd., 1-3-1 Edanishi, Aoba-ku, Yokohama 225-0014, Japan. <sup>2</sup> Department of Electronic Science and Engineering, Kyoto University, Nishikyo-ku, Kyoto 615-8510, Japan. <sup>3</sup> Photonics and Electronics Science and Engineering Center (PESEC), Kyoto University, Nishikyo-ku, Kyoto 615-8510, Japan. ✉email: [snoda@kuee.kyoto-u.ac.jp](mailto:snoda@kuee.kyoto-u.ac.jp)

Remarkable progress has been made in the development of high-power, broad-area, edge-emitting GaN-based semiconductor lasers, which can emit light of blue-violet-to-green wavelengths<sup>1–3</sup>. However, the oscillation of multi-lateral modes in these lasers significantly deteriorates their beam quality (and thus their brightness), which limits their range of applications. For example, they cannot be utilized directly for the processing (cutting, melting, and deforming) of difficult-to-process materials to which their lasing wavelengths are well-matched, such as copper and carbon fiber reinforced plastics (CFRP). Copper is an important material for electric cars, and CFRP is an important material for reducing the weight of cars and airplanes; thus, the machining of these materials with lasers is expected to contribute to future, carbon-neutral transportation. In addition, GaN-based semiconductor lasers can be applied to illumination including adaptive driving beam (ADB) and laser displays, but before doing so their beam quality should be significantly improved without compromising their high output power.

Employing the concept of the photonic-crystal surface-emitting laser (PCSEL)<sup>4,5</sup> is one of the most promising ways to greatly expand the applicability of GaN-based lasers. A GaN-based PCSEL can realize high-power, high-beam-quality operation owing to broad-area coherent oscillation at a singularity (e.g.,  $\Gamma$ ) point of its two-dimensional (2D) photonic crystal. In addition, various functionalities can be implemented by exploiting the peculiar features of the photonic crystal. GaN-based PCSELS were first demonstrated in 2008<sup>6</sup>. These PCSELS had a triangular-lattice photonic crystal with a GaN/air unit cell structure, and they were fabricated by a method employing a buried SiO<sub>2</sub> layer to retain the GaN/air structure. However, their output power was limited to 1 mW and their lasing threshold current density was as high as 67 kA cm<sup>-2</sup>; the main reasons for this poor performance were a weak photonic-crystal resonance effect and large structural disorders caused by the buried SiO<sub>2</sub> layer and the associated complicated fabrication process. Nevertheless, these devices achieved coherent 2D oscillation owing to the nature of their triangular lattice, wherein relatively strong 2D optical coupling was preserved in spite of the disorders (see Supplementary Note 1). After this initial work, another photonic-crystal fabrication method using a mass-transport phenomena<sup>7</sup> was reported, where the PCSEL had a square lattice structure. Unfortunately, this mass-transport method also deteriorated the uniformity of the GaN/air structure. Even worse, coherent 2D oscillation was not achieved because the 2D optical coupling could not be maintained by the square lattice (see Supplementary Note 1), resulting in cross-shaped, one-dimensional (1D) oscillations instead. These previous results revealed two issues inherent to wide-bandgap GaN-based materials: First, it is fundamentally difficult to obtain a strong 2D photonic-crystal resonant effect owing to the low refractive index contrast in wide-bandgap GaN systems; second, there lacks a method of embedding GaN-based nanostructures without introducing disorders inside the laser device. Without solutions to these issues, high-power, high-beam-quality operation of GaN-based PCSELS remained elusive.

In this paper, we address the above issues and realize sufficiently low-threshold-current-density, watt-class high-power, high-beam-quality operation in wide-bandgap GaN-based PCSELS. First, we design a device layer structure to enhance the 2D photonic-crystal resonant effect for the purpose of achieving a low threshold current density. Here, we employ a square-lattice photonic-crystal structure; although a square lattice exhibits weaker 2D optical coupling than a triangular lattice, the square lattice is superior to the triangular lattice for breaking the symmetry of the resonant electromagnetic field distribution (see Supplementary Note 1), which is important to realize a high-power, single-lobed beam as described later. Next, we develop a

nano-fabrication method for realizing a GaN/air structure with sufficiently small disorders. Based on these developments, we demonstrate lasing with a low threshold current density. Then, we design an asymmetric double-lattice structure whose two lattices are separated by  $0.46a$  (where  $a$  is the lattice constant) to enhance the extraction efficiency of laser light for high-power (and single-lobed) operation while maintaining a strong in-plane resonant effect. Based on these optimizations, we successfully realize GaN-based PCSELS capable of watt-class high-power, high-beam-quality operation and the emission of a circular, single-lobed with a very narrow divergence angle. With these PCSELS, we also demonstrate high-power, high-beam-quality continuous-wave (CW) operation.

## Results and discussion

### Design for enhancing resonance in GaN photonic crystals.

First, we design a structure to realize reasonably low-threshold-current-density operation of the GaN-based PCSEL. To clarify the main causes of the high threshold current density of the devices reported previous works<sup>6,7</sup>, we analyzed the magnitude of the loss of those devices by three-dimensional coupled-wave theory (3D-CWT)<sup>8</sup>. In our analysis, we focused on the in-plane optical loss from the edges of the photonic crystal, which was considered to be dominant since the output power of the PCSELS (associated with their vertical radiation loss, or their radiation constant) was very low. The in-plane losses for the PCSELS in references<sup>6,7</sup> were estimated to be 100 cm<sup>-1</sup> and 76 cm<sup>-1</sup>, respectively; these values are indicated by the black triangular and circular points in Fig. 1b. These large values clearly indicate that the strength of resonance inside the photonic crystal of the early devices was weak, which was mainly due to their immature designs, owing to the low refractive index contrast inherent to the wide-bandgap GaN-based materials. In order to enhance the strength of resonance, we adjusted the layer structure of the device to increase the optical confinement inside the photonic crystal layer, whose cross-section is shown schematically in Fig. 1a (see Supplementary Table 3 for further details). The in-plane loss was calculated as functions of the distance between the photonic-crystal layer and the active layer ( $d_{\text{PC-active}}$ ) and the resonator size; the results of these calculations are plotted in Fig. 1b as red, blue and green circles. It is seen that the in-plane loss is significantly reduced as  $d_{\text{PC-active}}$  is made smaller and as the resonator size is made larger. Thus, even using GaN-based materials, which have a low refractive index contrast, an appropriately designed optical confinement structure and resonator size can be employed to sufficiently reduce the in-plane loss. Note that previous experimental results had additional loss (namely, scattering loss) due to the large structural disorders. This scattering loss can be reduced by employing our nano-fabrication method, which is discussed in the next section.

### Establishment of a nano-fabrication method for GaN/air photonic crystals.

Previously reported fabrication methods<sup>6,7</sup> were beset by several serious issues toward realizing structurally uniform GaN/air photonic crystals. One method, which employed buried SiO<sub>2</sub> films<sup>6</sup>, introduced large structural disorders, mainly due to the complicated fabrication process involving the deposition of the SiO<sub>2</sub> film onto air holes formed in the GaN layer, which led to an increase of the scattering loss. In addition, material impurities might have been inadvertently introduced by the SiO<sub>2</sub> film and its associated deposition process, which would have affected the optical absorption and the electrical characteristics of the device. Another method, which utilized mass-transport phenomena<sup>7</sup>, suffered from the same problem of disorders, possibly due to the uncontrollability of the mass transport phenomena. Furthermore, using either method,

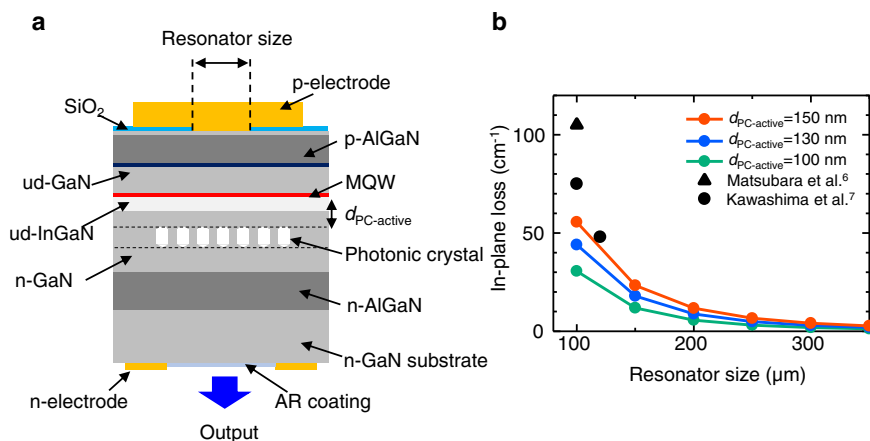


**Fig. 1** In-plane losses of GaN-based PCSELS. **a** Cross-sectional schematic of the GaN-based PCSEL structure. **b** 3D-CWT-based analysis of in-plane loss versus resonator size for a family of distances  $d_{PC-active}$  between the photonic crystal layer and the active layer.

the shape of the air holes was mostly symmetrical, which led to the cancellation of the vertical radiation field and thus a low output power.

Here, we propose and demonstrate a nano-fabrication method for GaN/air photonic crystals. Figure 2a–c show schematic images of our method, and Fig. 2d–f show corresponding scanning-electron-microscope (SEM) images of the fabricated structure. First, photonic crystals were fabricated by electron-beam lithography and reactive ion etching (RIE) (Fig. 2a, d). Then, a GaN layer was regrown on the patterned GaN layer without filling the air holes by metal-organic vapor phase epitaxy (MOVPE) with appropriately controlled deposition conditions (Fig. 2b, e), in which crystal growth was carried out in a temperature range where mass-transport phenomena did not occur. The surface above the air hole had a hexagonal pyramid-like concave shape due to the  $\{1\bar{1}01\}$  crystal facets. In order to flatten this surface, the temperature was raised and the growth mode was switched to the lateral direction. As a result, we succeeded in embedding air holes beneath a GaN film with a highly flat surface (Fig. 2c, f). Figure 2g, h show top-view SEM images of GaN/air photonic crystals after RIE and after regrowth, respectively, where the latter was observed after removing the regrown GaN layer by using a focused-ion beam (FIB). Interestingly, the air-hole shapes changed from circular to hexagonal with thermally stable  $\{1\bar{1}00\}$  facets, a reduced width (40 nm), and a high degree of uniformity. These results indicate the success of our nano-fabrication of GaN/air photonic crystal unit cell structures with very low disorders.

Next, we modified the unit cell structure based on the above nano-fabrication method. Considering that the shapes of the finished air holes have thermally stable  $\{1\bar{1}00\}$  facets, we etched elongated, asymmetric air holes along the  $\langle 11\bar{2}0 \rangle$  direction as shown in Fig. 2i, and then we repeated the nano-fabrication process described above. Figure 2j shows the top-view SEM image of the finished GaN/air unit cell, which was observed by removing the regrown GaN layer by FIB. As is seen in the figure, GaN/air holes having an asymmetric structure with thermally stable  $\{1\bar{1}00\}$  facets were successfully obtained. The asymmetry of this structure is important for realizing high output power as described later.

**Realization of low-threshold-current-density operation.** Here, we show that the threshold current density can be significantly reduced by utilizing the above design and nano-fabrication process. We fabricated a PCSEL with a square-lattice photonic crystal with symmetric hexagonal air holes as shown in Fig. 2h, where the layer structure shown in Fig. 1a was employed and the distance

between the photonic crystal layer and the active layer ( $d_{PC-active}$ ) was set to 150 nm. The fabrication process of this PCSEL is detailed in Supplementary Note 2. A Pd/Au circular p-electrode with a diameter of 200 μm was deposited on a p-GaN contact layer, and a Ti/Au ring-shaped n-electrode with an open aperture instead of a conventional uniform electrode<sup>6</sup> was deposited on the backside of the n-GaN substrate to improve light extraction. Figure 3a shows a microscope image of the finished device. The device was mounted on a package in the upside-down configuration, where the p-electrode can be seen through the aperture of the n-electrode. Figure 3b shows the optical output power as a function of the injected current density under room-temperature, pulsed conditions, where the pulse width and the repetition frequency were 100 ns and 1 kHz, respectively. For comparison, the output power of a previous PCSEL<sup>6</sup> is shown in the same figure. Evidently, we succeeded in realizing a dramatic reduction of the threshold current density, from  $\sim 67$  kA cm<sup>-2</sup> to  $\sim 2.6$  kA cm<sup>-2</sup>. Furthermore, we obtained an output power exceeding 200 mW. Figure 3c shows the far-field pattern (FFP) under an injected current density of 11 kA cm<sup>-2</sup>. The FFP was ring-shaped with a very narrow divergence angle of 0.28°, indicating that single-mode operation at the  $\Gamma$  point was achieved in spite of the large circular device area of 200-μm diameter. The ring-shaped beam reflects the symmetric unit cell structure of the device.<sup>9</sup> Namely, since the air hole had a symmetric hexagonal shape, the electromagnetic field distribution was also symmetric, causing destructive interference of the electric field at the center of the vertically diffracted beam and resulting in its annular shape.

### Realization of high-power single-mode operation

**Introduction of an asymmetric unit cell structure.** In the previous section, we succeeded in dramatically reducing the threshold current density and realizing a high output power exceeding 200 mW. In this section, we modify the air hole from a symmetric shape to an asymmetric one in order to alleviate the destructive interference of the electric field at the center of the vertically diffracted beam. In doing so, we realize a single-lobed beam with an even higher output power of >1 W.

Although there are various types of asymmetric air holes, including equilateral triangles<sup>9</sup> and right-angled isosceles triangles<sup>10</sup>, here we employ a double-hole structure in what is known as a double-lattice photonic crystal<sup>11</sup>. The double-lattice photonic crystal consists of two overlapping lattice groups separated by a distance of  $d$ , for the purpose of causing light diffracted in-plane by the individual lattice groups to optically interfere. When  $d$  is set to  $\sim a/4$ , this interference becomes

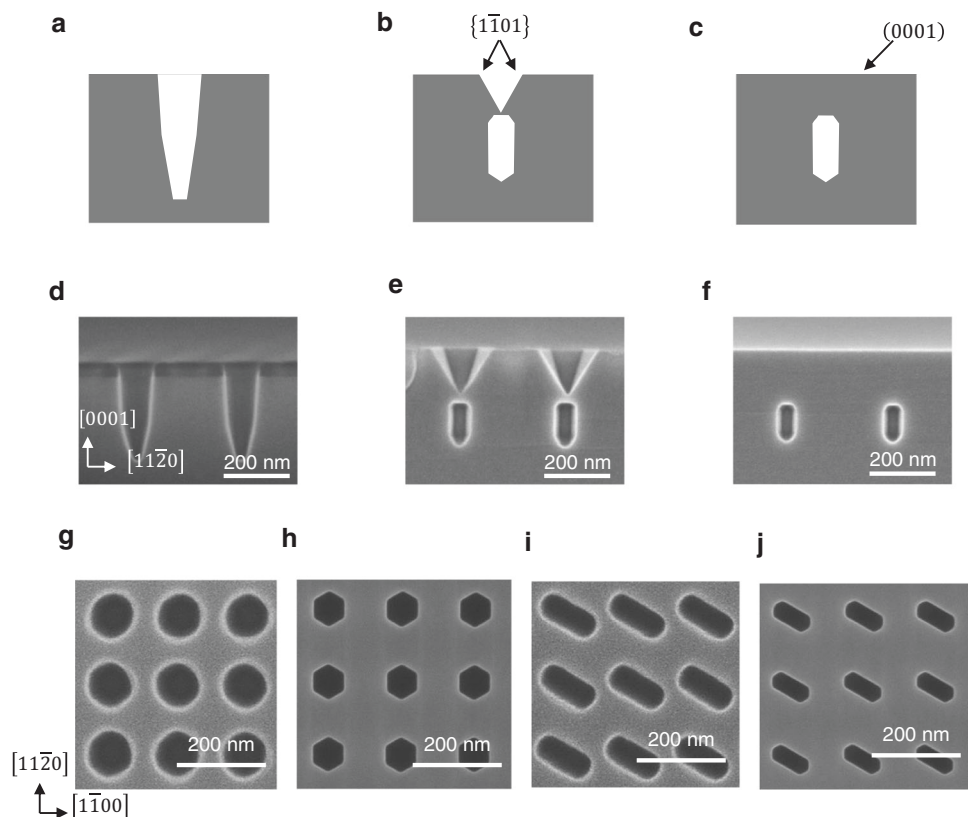


**Fig. 2 Nano-fabrication methods of GaN/air photonic crystals.** **a-c** Schematic of our nano-fabrication methods of GaN/air photonic crystals. **d-f** Cross-sectional SEM images of nano-fabrication methods of a GaN/air photonic crystal, corresponding to **a-c**. **g** A top-view SEM image of a photonic crystal with circular air holes after RIE. **h** A top-view SEM image of a photonic crystal after regrowth of **g**, observed by removing the top regrown GaN layer by FIB. **i** A top-view SEM image of a photonic crystal with elongated, asymmetric air holes along the  $\langle 11\bar{2}0 \rangle$  direction after RIE. **j** A top-view SEM image of a photonic crystal after the regrowth of **i**, observed by removing the top regrown GaN layer by FIB.

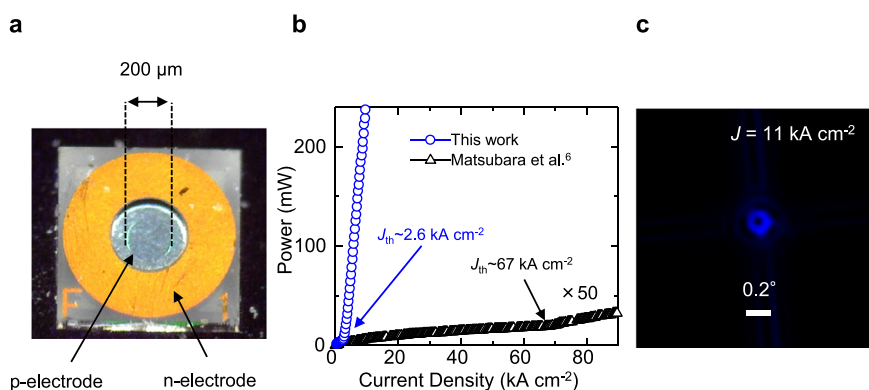


**Fig. 3 Lasing characteristics of a GaN-based PCSEL with single-lattice photonic crystals operated under pulsed conditions at room temperature.** **a** A microscope image of the finished device with a square-lattice photonic crystal with symmetric hexagonal air holes as shown in Fig. 2h and a circular current injection area with a diameter of 200  $\mu\text{m}$ . The backside p-electrode can be seen through the transparent GaN substrate. **b** Output power versus current density. **c** Measured far-field pattern under an injection current density of 11  $\text{kA cm}^{-2}$ .

destructive, which weakens the strength of in-plane optical confinement and thereby enables the oscillation of a single lateral mode even over wide resonator areas<sup>11</sup>. On the other hand, when  $d$  is set to around  $a/2$ , constructive interference occurs and in-plane optical confinement is strengthened<sup>11,12</sup>. In addition, the individual lattices can be given mutually different hole shapes and sizes, which increases the asymmetry of the overall structure and thus alleviates the destructive interference at the center of the

vertically emitted beam. Hence, by using a double-lattice structure, a single-lobed beam with high radiation constant is expected.

In the present work, we used two overlapping square lattices whose lattice separation  $d$  was set to  $0.46a$  as shown in Fig. 4a to achieve sufficiently strong in-plane confinement. For this structure, the radiation constant  $\alpha_v$  and the coupling coefficients  $\kappa_{1D}$  and  $\kappa_{2D}$  associated with in-plane coupling at angles of  $180^\circ$  and  $90^\circ$ , respectively, were calculated by 3D-CWT. The filling

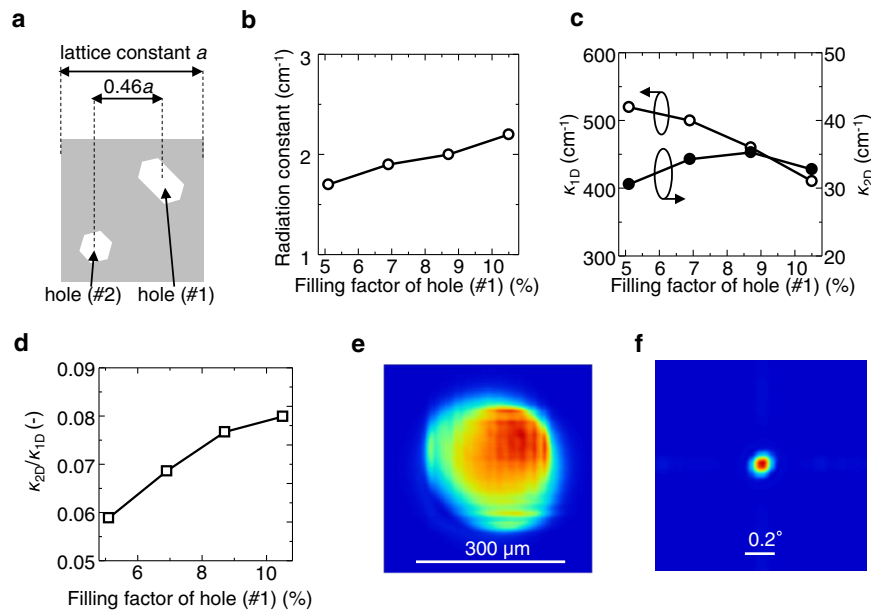


**Fig. 4** Design of a double-lattice photonic crystal and calculation of  $\alpha_v$ ,  $\kappa_{1D}$ ,  $\kappa_{2D}$ , near-field pattern and far-field pattern by 3D-CWT. **a** Schematic of a designed double-lattice photonic crystal. **b** Calculation of radiation constant  $\alpha_v$  versus FF of hole (#1). **c** Calculation of 1D coupling coefficient  $\kappa_{1D}$  and 2D coupling coefficient  $\kappa_{2D}$  versus FF of hole (#1). **d** Ratio  $\kappa_{2D}/\kappa_{1D}$  versus the FF of hole (#1). **e** Calculation of the NFP of a double-lattice structure using a FF of 10.5% for hole (#1) and 3.5% for hole (#2). **f** Calculation of the FFP of a double-lattice structure using a FF of 10.5% for hole #1 and 3.5% for hole (#2).

factor (FF) of one of the holes (#2) was fixed to 3.5%, while that of the other hole (#1) was set to several values (5.1%, 6.9%, 8.7%, and 10.5%). The layer structure was modified as detailed in Supplementary Table 5. Figure 4b shows the calculated radiation constant  $\alpha_v$  for each structure. Due to the effect of the asymmetry of the unit cell structure,  $\alpha_v$  was nonzero and it increased with increasing FF of hole (#1). Figure 4c, d show  $\kappa_{1D}$  and  $\kappa_{2D}$  as well as the ratio  $\kappa_{2D}/\kappa_{1D}$  as a function of the FF of hole (#1). As the FF increases,  $\kappa_{1D}$  decreases, while  $\kappa_{2D}$  tends to increase, leading to an increase of  $\kappa_{2D}/\kappa_{1D}$ . This relative increase of  $\kappa_{2D}$  over  $\kappa_{1D}$  is important to realize stable 2D oscillation (see Supplementary Note 3). Figure 4e, f show the calculated near-field pattern (NFP) and far-field pattern (FFP), which also took into account carrier-photon interactions<sup>13</sup>, when the FF of hole (#1) was set to its largest value (10.5%). The NFP reflects the asymmetry of the unit cell and has a nonzero central electric field (see Supplementary Note 4), and its corresponding FFP has the shape of a single circular lobe, as expected. Based on these results, we expect that high-output-power operation with a single-lobe beam is achievable by employing a double-lattice photonic crystal structure.

**Fabrication.** As discussed in the previous section, high-output-power operation with a single-lobed beam is expected by employing a double-lattice photonic crystal structure (Fig. 4a) with overlapping square lattices separated by a distance  $d$  of  $0.46a$ , where the air hole (#1) of one lattice has an elongated hexagonal shape, the air hole (#2) of the second lattice has a symmetric hexagonal shape (#2), and the two holes have different FF values. Although it already has been confirmed (Fig. 2h, j) that the structure of each individual lattice can be realized in experiments, it is not yet clear whether the two lattices can be overlapped without causing any deterioration of either structure. Figure 5a, b show top-view SEM images of the photonic crystals after RIE and regrowth, respectively, where the latter was observed by removing the regrown layer of GaN by FIB. It is confirmed in Fig. 5a that the double-lattice photonic crystal has been successfully fabricated even though the minimum feature size is only  $\sim 15$  nm. It is also confirmed in Fig. 5b that the final

double-lattice structure is very uniform and that the individual unit cells have FF values of 8.8% (#1) and 4.2% (#2), which are close to the designed values. Note that although the length of one side of the smaller hexagonal holes (#1) is only  $\sim 20$  nm, its standard deviation was found to be  $\sim 1$  nm, indicating that our nano-fabrication method is well-suited for realizing uniform double-lattice photonic crystal structures. Then, PCSELS were fabricated with the same process as described in the previous section, with the exception that the diameter of the Pd/Au circular p-electrode was expanded from 200  $\mu\text{m}$  to 300  $\mu\text{m}$ .

**Pulsed operation.** Figure 5c shows the output power-current characteristic of the finished device, where the pulse width and the repetition frequency were set to 100 ns and 1 kHz, respectively. The threshold current was  $\sim 2.1$  A, which corresponded to a threshold current density of  $\sim 3.0$   $\text{kA cm}^{-2}$ . An output power exceeding 1 W was obtained. In addition, operation in a single longitudinal mode was observed at a lasing wavelength at 431 nm as shown in Fig. 5d. The resolution of the spectrometer was 0.05 nm. The lasing band edge was confirmed to be band B (see Supplementary Fig. 7). Figure 5e shows the FFPs under injection currents of 4.0 A, 5.0 A and 6.5 A. It is seen that circular, single-lobed beams with very narrow divergence angles of  $\sim 0.15^\circ$  were successfully achieved. The very narrow single-lobed beams enable various optical systems bundled with the device to be simplified. For example, the beam is well-suited for combination with a Galvano (or MEMS) scanning system (see Supplementary Note 6 and Supplementary Movie 1, where a drawing of the character “8” was successfully achieved without any lens nor optical adjustments). Such simplifications widen the range of applications for PCSELS in the visible-wavelength regime.

**Continuous-wave operation.** We also expanded the operation of the developed PCSELS from pulsed conditions to continuous-wave (CW) conditions. The device structure itself was similar to the one used for pulsed operation. However, the p-electrode was changed from Pd/Au to ITO/Ag in order to improve the light extraction efficiency by reflecting a greater portion of light from the p-side into the

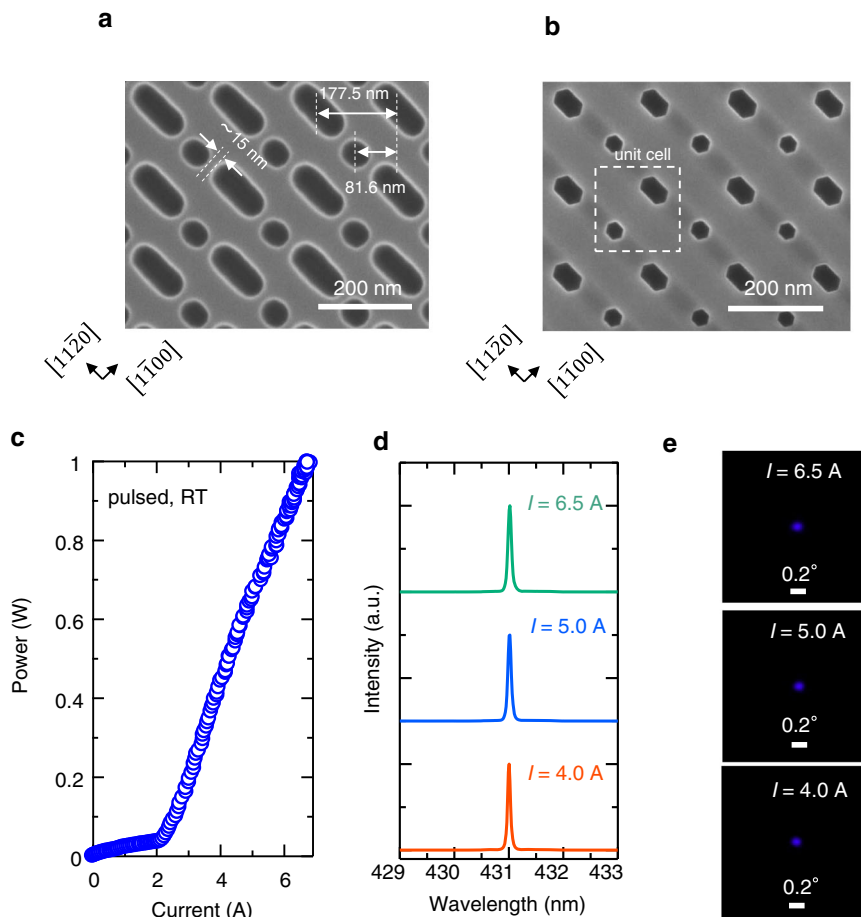


**Fig. 5** SEM image of double-lattice photonic-crystals and lasing characteristics of a GaN-based PCSEL with double-lattice photonic crystals under pulsed operation. **a** SEM image of double-lattice holes fabricated by dry etching. **b** SEM image of double-lattice photonic crystals after the regrown GaN layer is removed by FIB. **c** Output power as a function of current under pulsed operation at room temperature. **d** Emission spectra at injection currents of 4.0 A, 5.0 A and 6.5 A. The resolution of the spectrometer used for the measurements was 0.05 nm. **e** Measured far-field patterns at injection currents of 4.0 A, 5.0 A and 6.5 A.

n-substrate toward the optical facet (see Supplementary Table 6 and Supplementary Note 7 for details). The device was bonded to a heat sink to dissipate the heat generated during CW operation. Figure 6a, b, respectively, show the CW output power-current characteristic and the emission spectrum at an injection current of 5.0 A. The output power exceeded 320 mW even under CW conditions. Oscillation in a single longitudinal mode at a wavelength of  $\sim 438$  nm was also observed. The threshold current was  $\sim 3.8$  A, corresponding to a threshold current density of  $\sim 5.4$  kA cm $^{-2}$ , which was higher than that for pulsed operation. This was partly due to a slight mismatch of the resonant wavelength and the gain peak, which was caused by a rise of temperature during CW operation, and also due to a reduction of the lasing area as described below (see also the NFP), leading to an increase of the in-plane loss. Figure 6c, d show the NFP and the FFP, respectively. The NFP reveals that 2D lasing oscillation occurred in a localized circular area of  $\sim 235$   $\mu$ m diameter, which was mainly due to spatial nonuniformity of the band-edge frequency induced by a nonuniform in-plane temperature distribution during CW operation<sup>14</sup>. Uniform lasing oscillation over the entire device area can be realized by introducing a photonic-crystal structure with an artificially deformed lattice constant distribution that counterbalances the band-edge frequency distribution. In spite of the localized NFP, the FFP nevertheless exhibited a narrow, circular, single-lobe shape with a divergence angle of  $0.14^\circ$ . Considering its effective emission area, the beam was diffraction-limited (i.e., its beam quality  $M^2 \sim 1.0$ ). Thus, we may claim that we have achieved high-power single-mode oscillation even under CW conditions.

## Conclusions

We have realized watt-class high-power, high-beam-quality operation of GaN-based PCSELS with a lasing wavelength in the blue region. First, we have designed a device layer structure to enhance the 2D photonic-crystal resonant effect even using GaN-based materials, which have a low refractive index contrast, for the purpose of achieving low-threshold-current-density operation. Next, we have developed a nano-fabrication method for realizing GaN/air structures with sufficiently small disorders. Based on these developments, we have demonstrated lasing operation with a low threshold current density of  $2\text{--}3$  kA cm $^{-2}$ , which is more than one order of magnitude smaller than those of previous works. Then, we have introduced an asymmetric unit cell based on a double-lattice structure, whose two lattices were separated by a distance of  $0.46a$ , in order to enhance the extraction efficiency of lasing light toward the optical facet for high-power operation, and also to strengthen in-plane optical confinement. Based on these optimizations, we have succeeded in the development of a GaN PCSEL with high, watt-class ( $>1$  W) output power and a circular, single-lobe beam with a very narrow ( $\sim 0.2^\circ$ ) divergence angle. In addition, we have even demonstrated CW operation with a high output power ( $\sim 320$  mW) and a high beam quality ( $M^2 \sim 1$ ). This work is an important step toward implementing GaN-based semiconductor lasers in various applications including the processing of difficult-to-process materials, such as copper and CFRP, as well as high-brightness illuminations and displays and even subaquatic sensing and communications. Employing a double lattice structure with a lattice separation of  $d = 0.25a$  and broadening the

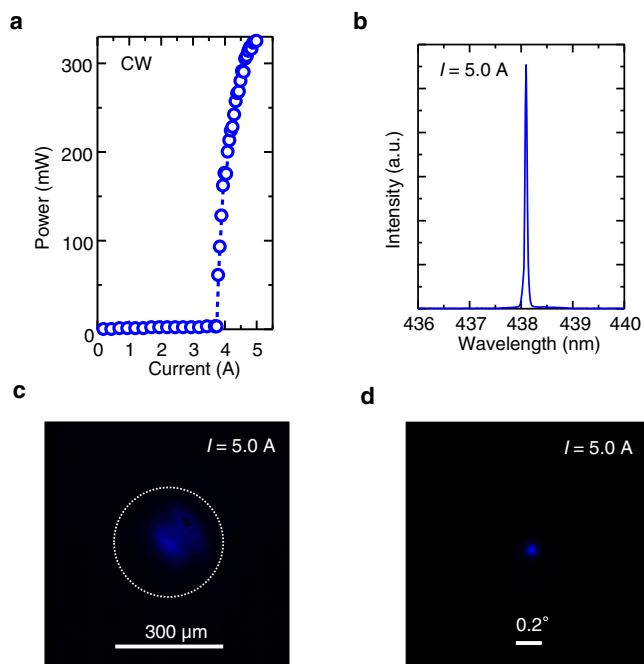


**Fig. 6** Lasing characteristics of a GaN-based PCSEL with double-lattice photonic crystals under CW operation. **a** Output power as a function of current under CW operation at 20 °C. **b** Emission spectrum under CW operation under an injection current of 5.0 A. The white dashed line indicates the current injection area. **c** Measured near-field pattern under CW operation at an injection current of 5.0 A. **d** Measured far-field pattern under CW operation at an injection current of 5.0 A.

resonator size to even larger (>1 mm) diameters would lead to the realization of even higher power (>10 W) operation while maintaining a high beam quality.

## Methods

The fabrication process of the GaN-based PCSEL was as follows. First, an n-side cladding layer and an n-side optical guiding layer were grown on a (0001) n-GaN substrate by metal-organic vapor phase epitaxy (MOVPE). Next, photonic crystal patterns were fabricated using electron beam (EB) lithography and inductively coupled plasma reactive ion etching (ICP-RIE). Then, the substrate was reloaded in the MOVPE chamber and a GaN layer was regrown on the patterned GaN layer without filling the air holes by our nano-fabrication method. Subsequently, a multiple quantum well layer, a p-side optical guide layer, an electron blocking layer, a p-side cladding layer and a contact layer were grown. Afterward, a SiO<sub>2</sub> film was deposited on the p-contact layer, except for over a circular region to be used for the current injection. Then, a p-contact electrode (Pd/Au or ITO/Ag) was deposited on the contact layer and covered by a Ni/Pd/Au pad electrode. Following these depositions, the GaN substrate was grinded and mirror polished by chemical mechanical polishing (CMP). A ring-shaped n-electrode (Ti/Au) and an anti-reflection coating were deposited on the backside of the GaN substrate.

**Reporting summary.** Further information on research design is available in the Nature Research Reporting Summary linked to this article.

## Data availability

The data that support the plots within this paper and other findings of this study are available within this Article and its Supplementary Information, and are also available from the corresponding author upon reasonable request.

## Code availability

All associated code for 3D-CWT simulations is available from the corresponding author upon reasonable request.

Received: 28 March 2022; Accepted: 9 September 2022;

Published online: 07 October 2022

## References

1. Michiue, A. et al. High-power pure blue InGaN laser diodes. *IEICE Trans. Electron.* **E92-C**, 194–196 (2009).
2. Kawaguchi, M. et al. Optical-loss suppressed InGaN laser diodes using undoped thick waveguide structure. *Proc. SPIE* **9748**, 974818 (2016).
3. Murayama, M. et al. Watt-class green (530 nm) and blue (465 nm) laser diodes. *Phys. Status Solidi A* **215**, 1700513 (2018).
4. Imada, M. et al. Coherent two-dimensional lasing action in surface-emitting laser with triangular-lattice photonic crystal structure. *Appl. Phys. Lett.* **75**, 316–318 (1999).
5. Noda, S., Kitamura, K., Okino, T., Yasuda, D. & Tanaka, Y. Photonic-Crystal Surface-Emitting Lasers: Review and Introduction of Modulated-Photonic Crystals. *IEEE J. Sel. Top. Quantum Electron.* **23**, no. 6, (2017).
6. Matsubara, H. et al. GaN photonic-crystal surface-emitting laser at blue-violet wavelengths. *Science* **319**, 445–447 (2008).
7. Kawashima, S. et al. GaN-based surface-emitting laser with two-dimensional photonic crystal acting as distributed-feedback grating and optical cladding. *Appl. Phys. Lett.* **97**, 251112 (2010).
8. Liang, Y., Peng, C., Sakai, K., Iwahashi, S. & Noda, S. Three-dimensional coupled-wave model for square-lattice photonic crystal lasers with transverse electric polarization: a general approach. *Phys. Rev. B* **84**, 195119 (2011).
9. Miyai, E. et al. Photonics: Lasers producing tailored beams. *Nature* **441**, 946 (2006).
10. Hirose, K. et al. Watt-class high-power, high-beam-quality photonic-crystal lasers. *Nat. Photon.* **8**, 406–411 (2014).
11. Yoshida, M. et al. Double-lattice photonic-crystal resonators enabling high-brightness semiconductor lasers with symmetric narrow-divergence beams. *Nat. Mater.* **18**, 121 (2019).
12. Inoue, T., Yoshida, M., De Zoysa, M., Ishizaki, K. & Noda, S. Design of photonic-crystal surface-emitting lasers with enhanced in-plane optical feedback for high-speed operation. *Opt. Express* **28**, 5050 (2020).
13. Inoue, T. et al. Comprehensive analysis of photonic-crystal surface-emitting lasers via time-dependent three-dimensional coupled-wave theory. *Phys. Rev. B* **99**, 035308 (2019).
14. Katsuno, S. et al. Self-consistent analysis of photonic-crystal surface-emitting lasers under continuous-wave operation. *Opt. Express* **29**, 25118 (2021).

## Acknowledgements

This work was carried out under the New Energy and Industrial Technology Development Organization (NEDO) and Council for Science, Technology and Innovation (CSTI), Cross ministerial Strategic Innovation Promotion Program (SIP), “Photonics and Quantum Technology for Society 5.0” (Funding agency: QST).

## Author contributions

S.N. directed this work with H.T. S.N. also designed this work. K.E. fabricated the device with K.I. and M.D.Z. T.K. performed epitaxial growth for the device. K.E. measured the device characteristics with T.K., M.H., M.J., K.I. and M.D.Z. T.I. and M.H. conducted the theoretical analysis of the device. K.E. and S.N. wrote the paper with discussions with T.K., T.I. and the other authors.

## Competing interests

The authors declare no competing interests.

## Additional information

**Supplementary information** The online version contains supplementary material available at <https://doi.org/10.1038/s43246-022-00288-6>.

**Correspondence** and requests for materials should be addressed to Susumu Noda.

**Peer review information** *Communications Materials* thanks Bernard Gil, Qifa Liu and the other, anonymous, reviewer(s) for their contribution to the peer review of this work. Primary Handling Editors: Klaas-Jan Tielrooij and Aldo Isidori. Peer reviewer reports are available.

**Reprints and permission information** is available at <http://www.nature.com/reprints>

**Publisher's note** Springer Nature remains neutral with regard to jurisdictional claims in published maps and institutional affiliations.



**Open Access** This article is licensed under a Creative Commons Attribution 4.0 International License, which permits use, sharing, adaptation, distribution and reproduction in any medium or format, as long as you give appropriate credit to the original author(s) and the source, provide a link to the Creative Commons license, and indicate if changes were made. The images or other third party material in this article are included in the article's Creative Commons license, unless indicated otherwise in a credit line to the material. If material is not included in the article's Creative Commons license and your intended use is not permitted by statutory regulation or exceeds the permitted use, you will need to obtain permission directly from the copyright holder. To view a copy of this license, visit <http://creativecommons.org/licenses/by/4.0/>.

© The Author(s) 2022